MDPI

Article

Design and Validation of New Methodology for Hydraulic Passages Integration in Carbon Composite Mechanisms

Maya Sleiman [1,*,†], Khaled Khalil [2], Adrian Olaru [3], and Samer AlFayad [4]

[1] University of Evry Val d'Essonne- UPSaclay/ KALYSTA Actuation; 40 rue de pelvoux 91000 Evry France; mayasleiman@ieee.com
[2] Laboratoire de Materiaux et Mecanique, ECAM - Rennes;Campus de Ker Lann 35170 BRUZ; Rennes France; khaled.khalil@ecam-rennes.fr
[3] National University of Science and Technology Politecnica Bucharest, Romania; adrian.olaru2301@upb.ro
[4] Université d'Evry Val d'Essonne-UPSaclay;36 rue de pelvoux 91080 Evry France; samer.alfayad@univ-evry.fr
* Correspondence: mayasleiman@ieee.org
† Current address: Université d'Evry Val d'Essonne-UPSaclay/ KALYSTA Actuation; 40 rue de pelvoux 91000 Evry.

Featured Application: The procedure is applied to assemble mechanisms manufactured with carbon composite materials and having hydraulic actuation.

Abstract: Humanoid robots have rapidly become the focus of research in recent years, with the most impressive humanoids being hydraulically actuated. This is due to the capacity of hydraulic actuation to provide simultaneous high forces with dynamic motion. The scarcity of hydraulic robots is mainly due to the difficulty in managing hydraulic pipes. Those decrease the robot's social acceptance, safety, and are the main source of leaks. Recently, there has been a new trend in hydraulically actuated robots that involves creating internal oil passages within the robotic parts to eliminate the need for external flexible tubes. Developing these parts using carbon composite materials provides an additional advantage of ensuring lightweight yet robust robotic parts. However, assembling hydraulically integrated parts is challenging due to the leakproof requirement and the high pressures involved. This article proposes a new, reliable, and effective method that ensures a strong, leakproof assembly. A mathematical model with 11 parameters describing the assembly zone and accounting for geometric, material characteristic parameters, and porosity has been developed. A numerical model was conducted to evaluate the effect of those parameters on the state of the assembly. Experimental validation was conducted to evaluate the assembly force. A satisfactory convergence between the mathematical model and the experimental results was observed with a maximum deviation of 20%.

Keywords: Assembly procedure, Hydraulic integration, Carbon composite assembly

Citation: Sleiman, M.; Khalil, K.; Olaru, A., AlFayad S. Design and Validation of New Methodology for Hydraulic Passages Integration in Carbon Composite Mechanisms. *Appl. Sci.* **2024**, *1*, 0. https://doi.org/

Received:
Revised:
Accepted:
Published:

1. Introduction

Recent years have witnessed a technological revolution in the field of humanoid robotics. This has led to advances in all the disciplines involved, particularly in actuation technologies. The choice of the actuating technology depends upon the application. In fact, electric actuators are typically used for light tasks, notably for humanoid robots designed for social interaction. On the contrary, hydraulic actuators are used when high force is required. For example, the humanoid robot ATLAS from Boston Dynamics [1], SARCOS from Carnegie Mellon University [2] and HYDROïD, a full-size humanoid under development from Paris Saclay [3] are hydraulically actuated as they are destined to perform heavy-duty tasks. HYDROïD has 36 hydraulically-actuated Degrees of Freedom consisting of multiple mechanisms designed to fit in a restrained volume to respond to an anthropomorphic design [4].

Amid this technological evolution, hydraulic actuation is proving its ability to provide a high force-to-weight ratio and a high force-to-volume ratio. Several advances have

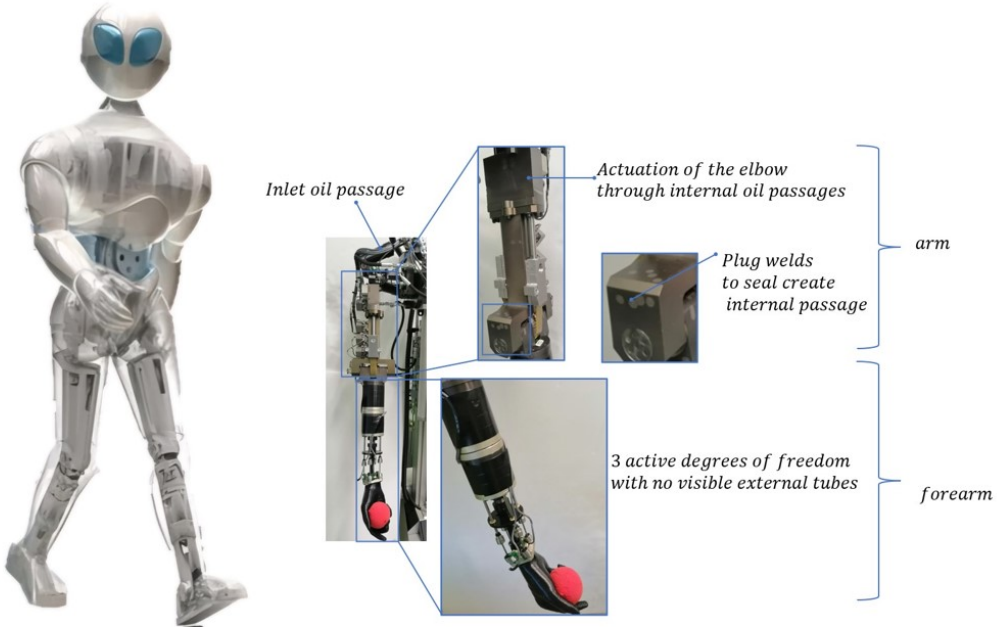

Figure 1. HYDROïD's arm and forearm-Integrated hydraulic tubes manufactured with conventional manufacturing processes

occurred in this domain where hydraulic cylinders became more electrically integrated and compact [5]. However, this technology requires the use of hydraulic tubes. The multitude of hydraulic tubes in humanoids has several disadvantages: they decrease their social acceptance, and the tubes face the danger of tearing off, which puts the global function of the system at risk. A compromise must therefore be found between the advantages and disadvantages of hydraulic actuation to maximise the effectiveness of this technology. One possible solution for eliminating hydraulic tubes is using decentralized hydraulic systems. This technology consists of integrating multiple electro-hydraulic actuators at joints to locally generate the required energy [6]. Another method consists of using a single hydraulic pump and integrating hydraulic pipes into the robotic parts to create internal oil passages. Three methods were defined for this purpose:

1. **Conventional manufacturing:** Typically, these processes start with the rough machining of metallic blocks to create external shapes, and then oil passages are drilled to form internal oil tubes. This process requires considerable labor, resulting in high machining times and costs. The first generation of HYDROïD - V1 with full hydraulic integration was manufactured using conventional technologies mainly from steel, titanium, and aluminum. This work became more challenging when hybrid (Serial + parallel) mechanisms are involved which added to the complexity of the integration [7]. Referring to the figure 1, a high-pressure tube fed the robot arm at the shoulder, and the drilled tubes fed the arm and forearm joints internally [8]. The process supplies oil to all 36 hydraulically actuated active joints. Once the manufacturing process was complete, post-processing for corrosion protection or hardening was required, which added cost and time to the initial process. However, this manufacturing process is lengthy and costly and adds to the complexity of the design to take into account the feasibility of the manufacturing processes.

2. **Metal additive manufacturing:** With advances in manufacturing processes and materials, additive manufacturing has emerged as a new approach to designing portable devices. This technology allows the development of intricate shapes in which hydraulic oil passages can be pre-designed and printed within the structure. In 2016, Boston Dynamics announced that the next generation of ATLAS would incorporate

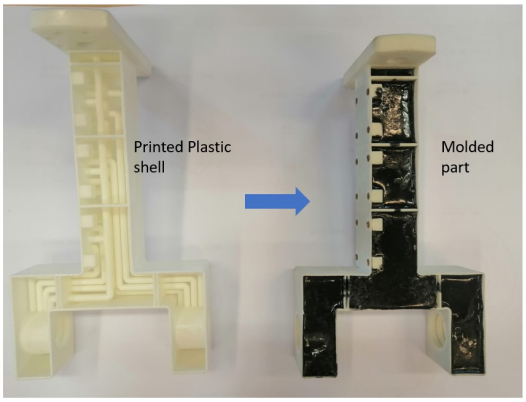

Figure 2. HYDROïD's arm manufactured with 3D-PPRCFRP (ElAsswad et al. [11]); printed shell part has three layers of tubes; it is then molded with carbon composite materials.

structures manufactured with additive manufacturing [9]. The robot leg housed a hydraulic cylinder barrel and valve emplacements. Following the same logic, a smart integrated actuator was developed in IIT-Italy. It was printed with Titanium alloys to permit the complex shapes to be made. The all-in-one actuator included integrated hydraulic paths, wire channels, valve emplacements, and position, force, and temperature sensors[10]. However, this technology requires post-processing of the material for stress relief and porosity elimination, which renders it ineffective in terms of cost and time.

3. **3D- Pre-Printed Random Carbon Fiber Reinforced Plastic - 3D-PPRCFRP:** In 2018, El-Asswad et al. proposed the 3D-PPRCFRP (3D- Pre-Printed Random Carbon Fiber Reinforced Plastic) methodology. This method enables the production of integrated hydraulic robotic parts by combining additive manufacturing and carbon composites. The process begins with printing a shell-shaped structural robotic part in plastic, with internal passages for oil and electrical wires. The shell-shaped part is then infused with randomly oriented carbon composite particles to increase its ability to withstand high pressures and forces. Figure 2 shows the second generation of HYDROïD's arm manufactured using this developed technology, with the printed shell part comprising three layers and a total of 14 internal oil passages. The process led to reducing the weight of the robotic parts by 85%, significantly reducing manufacturing time and cost [11]. The combination of additive manufacturing and composites resulted in a groundbreaking technology that provided a cost-effective way to produce hydraulically integrated components, overcoming the limitations of previous technologies.

The 3D-PPRCFRP has the most advantages compared to conventional and additive manufacturing methods. Carbon-reinforced plastics contribute to the reduction in the weight of mechatronic components. Firstly, lightweight materials improve energy efficiency by reducing the power required to move the device. This has a positive effect on extending the battery life, which increases autonomy. Secondly, lightweight humanoids promote safety, the lighter they are, the easier they are to control, which reflects positively on risk reduction and cost optimization. Despite being lightweight, carbon-reinforced materials are also strong, which can be translated into a high strength-to-weight ratio. Consequently, carbon composite material offers high design flexibility and the capacity to develop complex shapes through molding, optimizing the device's form and weight.

2. Problematic

As a recently introduced manufacturing technique, the assembly process of components produced with this method is yet to be investigated. Referring to Figure 3, parts A, B, C, and D are manufactured with 3D-PPRCFRP; while part E is a commercially available servovalve. The internal oil passages (3) are made of plastic (1) and reinforced with

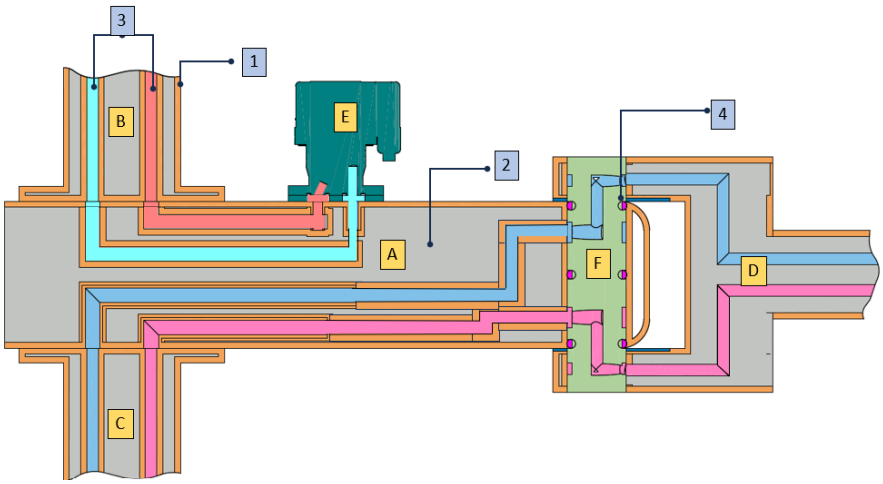

Figure 3. A, B, C, D, F parts are manufactured with 3D-PPRCFRP ; E is a commercial hydraulic valve. A, B, C, and E are fixed statically while parts A, F, and D are allowed to rotate in relation to each other. 1- Plastic shell; 2- composite material, 3- Internal oil paths; 4- Hydraulic seal.

composite material (2), with more than one passage passing between the parts. A typical mechanism comprises multiple parts that are either statically assembled, such as parts A/B, A/C, and A/E, or dynamically assembled, such as A/F/D. Dynamically assembled parts are leakproof due to hydraulic seals (4). But statically fixed assemblies must withstand the working forces while conserving the leakproof capacity. Challenges arise, particularly when integrating off-the-shelf components such as sensors and servo valves (E), which require precise surface finishing to prevent leakage. Consequently, the assembly procedure for the humanoid parts must be easy to perform and maintain, adaptable for the hydraulic application, and have a long service life. The study of the assembly zone includes various critical factors that should be considered. i) Material resistance in which the maximum forces the material can support are identified. ii) Manufacturing defects and surface finishing. In fact, deviations from the required tolerances can be sources of leak or stress concentrations, leading to fractures. iii) Temperatures can affect the material by causing expansions or retractions, leading to assembly failure. iv) Aging of the material can cause degradation in the long term, especially since these components are exposed to oil and moisture. v) Leak at high pressures. Including these domains in one multi-physics mathematical model is complex, but it allows a better understanding of the assembly procedure and a comprehension of the parameters involved.

3. Existing solutions

Several assembly solutions for parts manufactured with composite materials can be envisaged such as direct threading, bonding, or metallic inserts.

- **Direct threading:** Direct threading is generally used for metallic component assembly. Several researches were conducted to study the effect of drilling and tapping parameters on the tools and the resulting force at the assembly [12] [13] in composite materials. It has been concluded that the tool is highly affected by the number of drills made per tool, which negatively influences the dimensions of the hole. Adding to that, due to the wear of the tools, the thread parameters are inconsistent, which reflects an inconsistency in the allowable forces supported by the assembly. This has led to additional research in order to reduce the tool wear and defects such as burr caused in the drilled material by using hybrid composite material, for example, aramid (C-AFRP) [14]. Other studies are working on applying Artificial Neural Network to predict the adequate machining parameters such as spindle rotation speed and feed rate [15]. Direct threading has a major drawback. In case of thread failure, the part

cannot be repaired, and a replacement of the full part might be necessary.

- **Adhesive bonding:** Ebnesajjad et al. [16] explored adhesive bonding to assemble parts manufactured with carbon composite materials. This method allows for a large stress-bearing area and a uniform distribution of stresses. However, there are drawbacks: i) assessing the bond area is impractical; ii) extensive surface preparation is required to ensure an adequate bond; iii) the use of tools like autoclaves and presses can complicate the assembly process, and iv) assembly takes a long time to allow for complete curing.

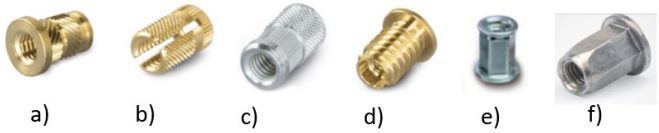

Figure 4. Commercial inserts types ultrasonic(a), expansion(b),press in(c), self tapping(d), molded in(e), and rivet nut inserts(f)- Image courtesy Bollhoff.

- **Metallic inserts:**
  Metallic thread inserts shown in Figure 4 are suitable for non-permanent assembly solutions. They are mainly used for plastic, wood, or aluminum assembly applications. Those inserts have external knurls to grip the material of the part they assemble. Replacing those described inserts will eventually result in permanent deformation of the parts, compromising the interchangeability requirement. Additionally, the external knurls cause irregular deformations that compromise the leak tightness requirement in a hydraulically integrated component.

4. Proposed solution

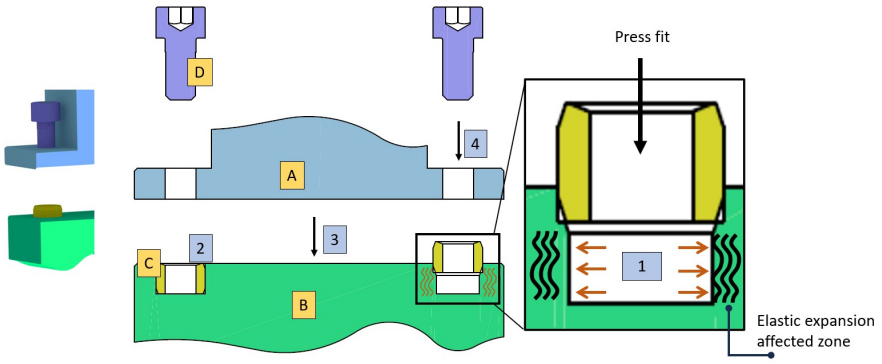

Figure 5. A & B are the parts to be assembled; C: intermediate, D: screw; 1- Expanding the composite material; 2- Inserting of the intermediate part, 3- Assembling the two parts; 4- Assembling the screw.

Having concluded that the existing solutions do not respond to the assembly requirements, a new solution is proposed in this section. The developed assembly procedure consists of three steps: i) A local modification in the material characteristics at the assembly place, ii) an internally threaded intermediate implementation, and iii) a threaded element to assemble the parts[17]. To comply with the hydraulically actuated humanoid robots assembly mentioned in section 2, the procedure must acquire:

1. High strength capacity: During hydraulic system operation, axial forces can cause the assembled parts to separate.
2. Replaceability: The intermediates must not damage the composite material when they are replaced.

3. Leakproof capacity: Hydraulic actuation systems require tightness characteristics. The mechanism's mounting surface must be flat and smooth. T
4. Light in weight: Robotic mechanisms usually need multiple fasteners for assembly. This increases the assembly time and compromises the system's lightweight requirements.

The proposed solution is based on **Elastic expansion** of the composite material; **Press fitting** the intermediate in the expansion, and **Assembling** with a threaded element, notably a screw which creates a suitable **Technology** for **Hydraulic integration - (EPATH)**. The assembly of parts A and B is explained in Figure 5, where the EPATH solution is applied. First, the expansion process occurs to the composite material (1), allowing for the intermediate (C) to be pressed (process 2). Part A is then fixed at the surface of part B (process 3) using the screws (D) (process 4).

5. Mathematical modeling of EPATH

The mathematical modeling of the EPATH procedure is crucial. It evaluates the force that holds the assembly zone function of geometric and material-related parameters. This allows for a better comprehension of the system and an evaluation of the parameters involved.

5.1. Concept description

The EPATH solution utilizes elastic expansion to fit the intermediate inside composite materials. Figure 6 shows a cross-section of an intermediate pressed inside a composite tube. The internal tube's radius R_{i2} is smaller than the external radius of the intermediate R_{o1}. This difference in diameters allows the composite material to expand elastically and grip into the intermediate, which increases the resistance to axial forces.

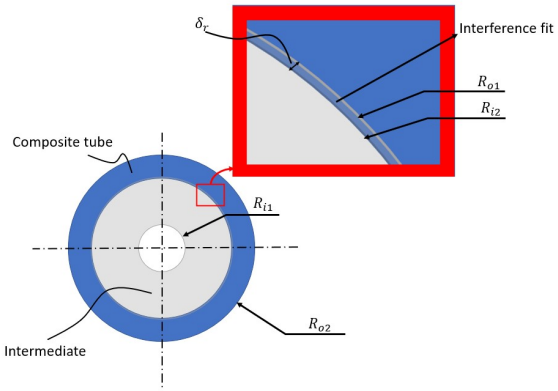

Figure 6. Parameters in the interference fit assembly, intermediate's internal radius R_{i1}, intermediate's external radius R_{o1}, Composite's internal radius R_{i2}, Composite's external radius R_{o2}, Interference fit radius R.

Based on Lame equations for thick-walled cylinders under pressure, the interference fit assembly is modeled [18]. The intermediate is considered a cylinder under external pressure, and the composite part is a cylinder under internal pressure.

The EPATH modeling consists of identifying the maximum axial force that holds the assembly. Consequently, parameters controlling the model are classified into four categories:

- Material: The elastic property of the composite material E_{comp} plays a significant role in defining its maximum allowable expansion at the interference fit zone.
- Geometric: The model takes into consideration dimensional parameters that include the intermediate's radii (Internal R_{i1} and external R_{o1}) as well as the composite mate-

rial (Internal R_{i2} and external R_{o2}). They also include the interference fit contact length l.

- Friction coefficient: The composite material and the intermediate are in full surface-to-surface contact at the interference fit zone. The maximum allowable thrust force is then a function of the friction coefficient μ_K between the two materials in contact.
- Composite material fill rate k: One of the main challenges in the composite molding process is the air bubbles. The high viscosity of the mixture traps the bubbles inside, weakening the structure and decreasing the effective working area.

5.2. Mathematical model

The radial interference fit is computed as a function of nominal radius R and the hoop strains in the intermediate ϵ_{t1} and the composite ϵ_{t2} [18]:

$$\delta_r = R(\epsilon_{t2} - \epsilon_{t1}) \tag{1}$$

The mathematical model will then start with the development of radial and hoop stresses (Equations 2 and 3) in thick walled cylinders calculated through the application of boundary conditions on the Lame's equations. This permits to determine Lame's constants A and B for the intermediate and the composite material [18]:

$$\sigma_r = A - \frac{B}{r^2} \tag{2}$$

$$\sigma_t = A + \frac{B}{r^2} \tag{3}$$

where r is a variable radius.

$$R_{i1} < r < R_{01} \tag{4}$$
$$R_{i2} < r < R_{02} \tag{5}$$

At the interference fit radius, once the elastic expansion is accomplished,

$$R = R_{o1} = R_{i_2} \tag{6}$$

Since both intermediate and composite hole have open ends, $\sigma_z = 0$. Lame's constants are now calculated for the intermediate and the composite material considering the boundary conditions:

◇ Concerning the intermediate: At its internal diameter, the radial stress is null, $\sigma_r = 0$ $A_1 - \frac{B_1}{R_{i1}^2} = 0$ therefore

$$A_1 = \frac{B_1}{R_{i1}^2} \tag{7}$$

At the interference fit radius R, the radial stress is equal to the negative pressure: So $\sigma_r = -P$

$$A_1 - \frac{B_1}{R^2} = -P \tag{8}$$

by replacing A_1 by its value we obtain:

$$A_1 = -\frac{PR^2}{R^2 - R_{i1}^2} \tag{9}$$

$$B_1 = -\frac{PR_{i1}^2R^2}{R^2 - R_{i1}^2} \tag{10}$$

◇ Concerning the composite material: At its outer diameter, no pressure is applied $\sigma_r = 0$, therefore

$$A_2 = \frac{B_2}{R_{o2}^2} \tag{11}$$

At the interference fit radius R the radial stress is equal to the negative pressure: So $\sigma_r = -P$

$$A_2 - \frac{B_2}{R^2} = -P \tag{12}$$

by replacing A_2 by its value we obtain:

$$B_2\left(\frac{1}{R_{o2}^2} - \frac{1}{R^2}\right) = -P \tag{13}$$

Therefore

$$B_2 = -\frac{PR_{o2}^2R^2}{R^2 - R_{o2}^2} \tag{14}$$

$$A_2 = -\frac{PR^2}{R^2 - R_{o2}^2} \tag{15}$$

Applying HOOK's law at a plane strain state the hoop strain at the intermediate is: $\epsilon_{t1} = \frac{1}{E_i}(\sigma_{t1} - v_i\sigma_{r1})$

$$\epsilon_{t1} = \frac{1}{E_i}\left[-\frac{P}{1 - \frac{R_{i1}^2}{R^2}} - \frac{PR_{i1}^2}{1 - R^2\left(\frac{R_{i1}^2}{R^2}\right)} - v_i\left(-\frac{P}{1 - \frac{R_{i1}^2}{R^2}} + \frac{PR_{i1}^2}{1 - R^2\left(\frac{R_{i1}^2}{R^2}\right)}\right)\right] \tag{16}$$

$$\epsilon_{t1} = \frac{1}{E_i}\left[-\frac{P}{1 - \frac{R_{i1}^2}{R^2}}\left(1 + \frac{R_{i1}^2}{R^2}\right) + v_i\frac{P}{1 - \frac{R_{i1}^2}{R^2}}\left(1 - \frac{R_{i1}^2}{R^2}\right)\right. \tag{17}$$

Therefore

$$\epsilon_{t1} = \frac{P}{E_i}(-W_i + v_i) \tag{18}$$

where

$$W_i = \frac{R^2 + R_{i1}^2}{R^2 - R_{i1}^2} \tag{19}$$

$$\epsilon_{t2} = \frac{1}{E_{comp}}\left(\sigma_{t2} - v_{comp}\sigma_{r2}\right) \tag{20}$$

$$\epsilon_{t2} = \frac{1}{E_{comp}}\left[-\frac{P}{1-\frac{R_{o2}^2}{R^2}} - \frac{PR_{o2}^2}{1-R^2\left(\frac{R_{o2}^2}{R^2}\right)} - v_{comp}\left(-\frac{P}{1-\frac{R_{o2}^2}{R^2}} + \frac{PR_{o2}^2}{1-R^2\left(\frac{R_{o2}^2}{R^2}\right)}\right)\right] \tag{21}$$

$$\epsilon_{t2} = \frac{1}{E_{comp}}\left[-\frac{P}{1-\frac{R_{o2}^2}{R^2}}\left(1+\frac{R_{o2}^2}{R^2}\right) + v_{comp}\frac{P}{1-\frac{R_{o2}^2}{R^2}}\left(1-\frac{R_{o2}^2}{R^2}\right)\right] \tag{22}$$

Where the Young modulus of the composite material is calculated through the rule of mixture for reinforced composite materials [19]: $E_{comp} = K_f E_f \nu_f + E_m \nu_m$; where ν is the volume fraction coefficient and the subscript f refers to the particles, the subscript m refers to the matrix; the volume fraction coefficient of fiber is $\nu_f = 1 - \nu_m$ and k_f is the particle efficiency parameter. Its value is $k_f = \frac{1}{5}$ for discontinuous randomly oriented particles in space [19]. Assuming that the material is homogeneous and no porosity is present:

$$\epsilon_{t2} = \frac{P}{E_{comp}}\left(-W_{comp} + v_{comp}\right) \tag{23}$$

where

$$W_{comp} = \frac{R^2 + R_{o2}^2}{R^2 - R_{o2}^2} \tag{24}$$

By replacing equations (18) and (23) to the equation (1) we obtain the radial interference fit:

$$\delta_r = RP\left[\frac{1}{E_{comp}}\left(-W_{comp} + v_{comp}\right) + \frac{1}{E_i}\left(W_i - v_i\right)\right] \tag{25}$$

The pressure at the interference fit zone is then calculated:

$$P = \frac{\delta_r}{\left[R\left(\frac{1}{E_{comp}}\left(-W_{comp} + v_{comp}\right) + \frac{1}{E_i}\left(W_i - v_i\right)\right)\right]} \tag{26}$$

Knowing that the pressure resulting from the interference fit should overcome every pressure created by the applied force and torques as shown in figure 7, we can consider that [20]:

$$P \geq \frac{F}{2\pi R l \mu_K} \tag{27}$$

where F is the applied axial force, and l the length of the intermediate.

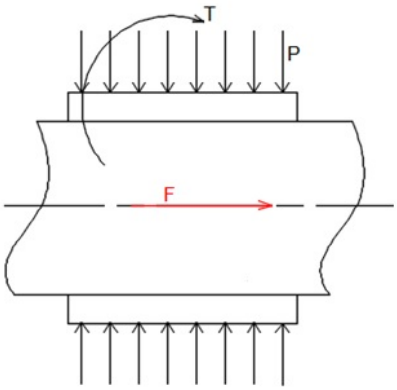

Figure 7. Force F and Torque T applied on the intermediate. Pressure created at the interference fit is represented P

The Push Through Force (PTF) is then equal to this force.

$$F = PTF = 2\pi RlP\mu_K \tag{28}$$

Referring to the equation 28, we can identify 11 variables.

$$PTF = f(R, R_{i1}, R_{o2}, l, E_i, E_f, E_m, \nu_k, \nu_f, \nu_i, \nu_{comp}) \tag{29}$$

Each parameter has a different impact on the PTF value. Their effect is studied numerically in the upcoming section.

6. Numerical validation

The numerical validation of the mathematical model is conducted in this section using MATLAB. It permits the identification of the impact of the 11 parameters on the PTF.

The composite material properties used in the experimental validation are obtained using specimens according to ISO 527-4 [21]. This allows for a more realistic numerical simulation. Therefore, rectangular specimens are designed and molded according to the ISO standard. They are then placed on a universal testing machine, and a traction force is applied. The test is conducted until the specimen is fractured. The elongation of the specimen and the force are registered. The 10% carbon composite properties are given in table 1.

Table 1. Carbon composite characterization; Traction test results.

Characteristic	Value	Unit
ν_f	10	%
Stress at fracture	28	*MPa*
Theoretical Young Modulus	2.6	*GPa*
Experimental Young Modulus	2.66	*GPa*
Young Modulus- Deviation	2.3	%
Strain at fracture	0.6	%

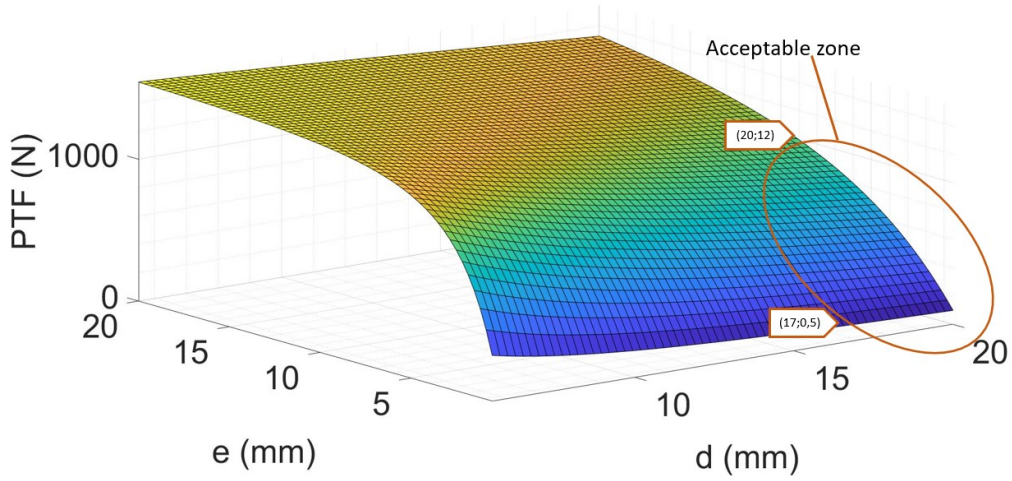

Figure 8. PTF represented as a function of the nominal diameter d and the thickness of the composite material e for a 10% volume fraction coefficient and 0.04mm radial interference fit. The intermediate used for the simulation is made of Steel. The acceptable range of PTF is marked inside the red area.

Referring to Figure 8, a numerical simulation was conducted to determine the effect of the nominal diameter d and the composite thickness $e = R_{o2} - R_{i2}$ on the PTF value that the EPATH assembly can support. The intermediate's material is steel. The acceptable range of PTF is marked inside the red area. It is defined by the maximum stress that the composite material can support. It can be noticed that the thickness of the composite e and the nominal diameter d play a major role. It is obvious that when e increases, PTF increases. Also, at the same nominal diameter, PTF becomes constant after a certain value of e. This allows for the optimization of the design of the robotic part and avoids over-dimensioning.

Numerical simulation of the Von Mises stresses, and the Push Through Force for 10% volume fraction coefficient of carbon particle are plotted in (a,b) for steel intermediates, (c,d) for brass intermediates, and (e,f) for aluminum intermediates and shown in Figures(9). The limit line of the admissible Von-Mises stresses is drawn based on the values of the maximum stresses found in the traction test (Table 1). It can be noticed that the Push Through Force (PTF) is higher when the interference fit value (δ_r) is higher and the nominal diameter (d) is lower. A combination of (δ_r, d) that creates stresses above the limit line causes plastic deformation of the composite material or even breaks it. Therefore, the choice of (δ_r, d) is then done from the acceptable area in the graph.

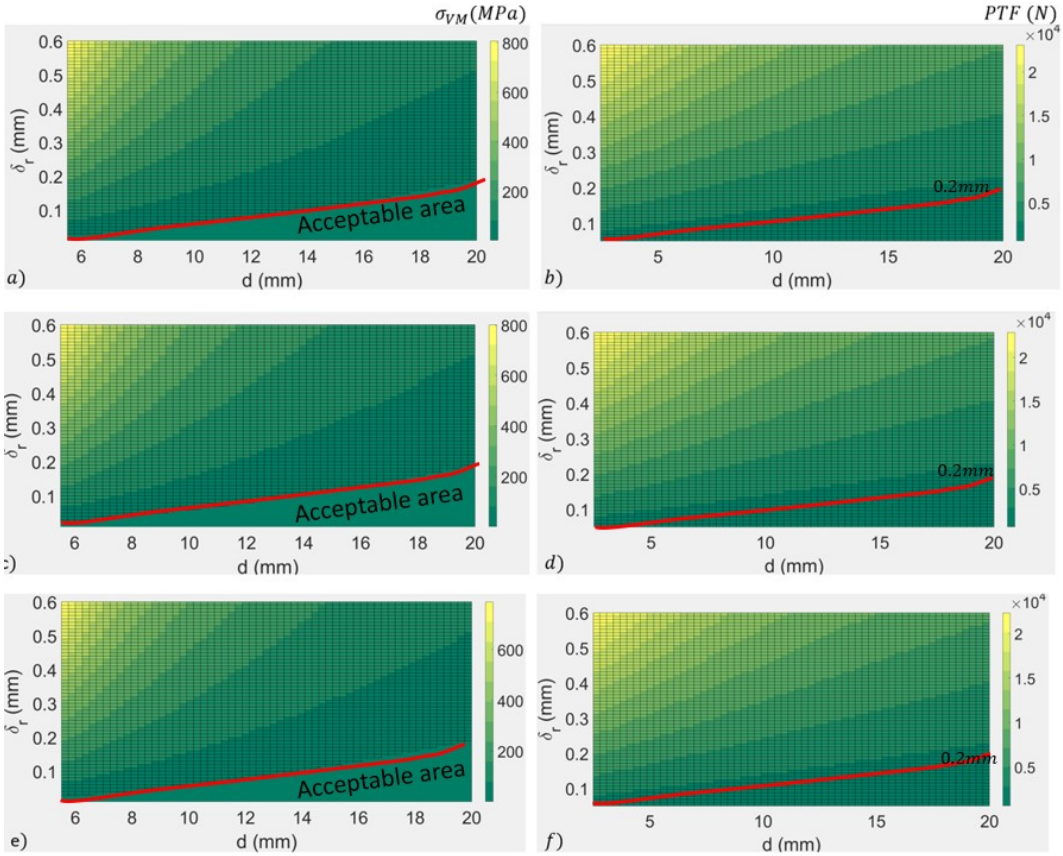

Figure 9. Acceptable values of the radial interference fit for a 3mm thickness of composite with $v_f = 10\%$ for steel intermediates (a,b), brass intermediates (c,d), and aluminum intermediates (e,f).

7. Experimental validation- Leak Proof test

The developed intermediates are destined to assemble two hydraulically integrated parts. Therefore, the intermediates must comply with the leakproof requirement. An experimental validation test is then essential to evaluate the assembly's capacity to remain leakproof during the functioning of the hydraulic system.

Specimens consisting of plastic cube shells are printed. They are then filled with composite material. The molded part is then drilled for an oil passage. An intermediate is pressed perpendicularly to the surface to receive high pressure from the drilled channel (Figure 10). Pressure is increased progressively until the burst of the molded specimen. The highest reached pressure was 100 bars. The tested specimens did not show any leak around the intermediates.

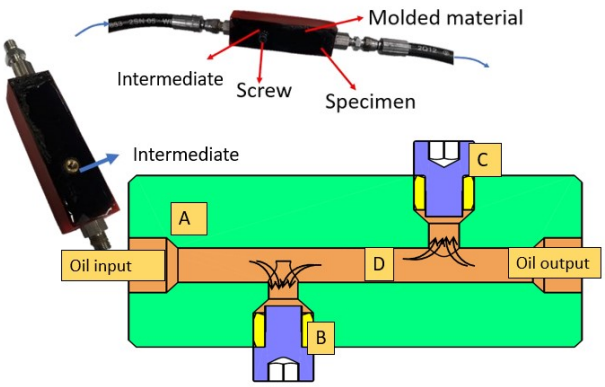

Figure 10. Leak test- A- tested specimen, B- Intermediate, C- Screw, D- Pressurized oil

8. Experimental validation- Evaluation of the PTF

The required force to push the intermediate from its position; the PTF is experimentally validated in this section. Therefore, specimens of carbon composite tubes with pressed intermediates were prepared. The intermediate was pushed from its emplacement on an MTS universal testing machine. The displacement of the intermediate and the force applied are then registered and plotted.

8.1. Specimen preparation

The specimen preparation for the PTF validation test underwent several steps : i) 155mm long tubes were designed and printed with PLA as shown in Figure 11-a. ii) Then randomly oriented carbon composite specimens were molded inside them with 10% volume fraction coefficient. The molding procedure was delicate due to the high exothermic curing process, which can cause mold deformation and the creation of air bubbles. Therefore, carbon particles were first mixed in the resin to ensure a full wet out of the particles. Then the hardener was added at a $100 - 30$ weight proportion(following the manufacturer's recommendation [22]). The mixture (resin-carbon particle) was degassed in the degassing chamber to release air bubbles created during the mixing procedure. After adding the hardener, the new mixture was degassed again. The entire mixture of epoxy carbon particles was allowed to cure at room temperature for two days (Figure 11-b). iii) The plastic/composite tubes were machined to create small cylinder tubes. The internal diameter is made to the tolerance d H7 ($d - 0.018mm$; for diameters up to 18 mm) (Figure 11-c). To create an interference fit, metallic intermediates were manufactured (brass, steel, aluminum) with an external diameter $d + 2\delta_r$ (Figure 11-d), then pressed inside the composite tubes to create the assembly of the full specimen(Figure 11-e). These specimens will be used in the PTF test.

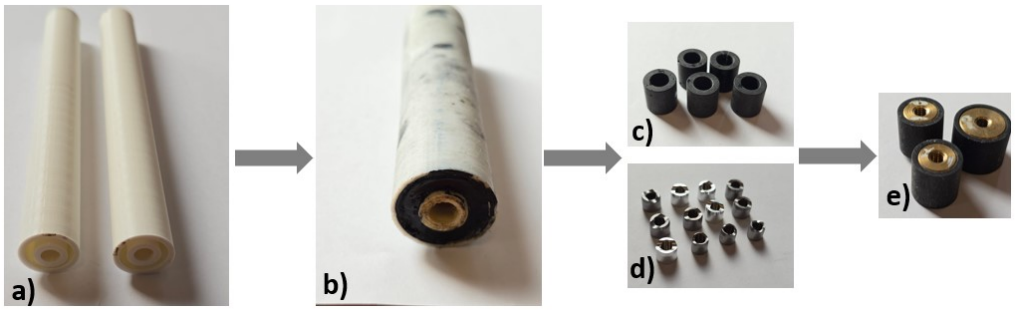

Figure 11. Steps for specimen preparation- a) PLA 3D printed hollow tubes used as molds; b) Carbon composite material molded inside PLA tubes; c) The molds are turned into small cylinders to host intermediates, and d) intermediates are machined at different diameters; e) intermediates are pressed in composite tubes in a press fit assembly and ready for test

8.2. Test description

The test's purpose is to apply a force at the top surface of the intermediate to push it from the composite tube. Therefore, new supports were developed for the MTS-100KN universal testing machine (Figure 12). The new upper support has a cylindrical extremity that will be applied on the top part of the intermediate to pull it down. It was attached to the moving part of the machine. The lower one serves as a support for the assembly. The upper jaw moved at the speed of $2mm/s$ and pushed the intermediate. The displacement and applied force to push the intermediate inside the composite tubes were recorded.

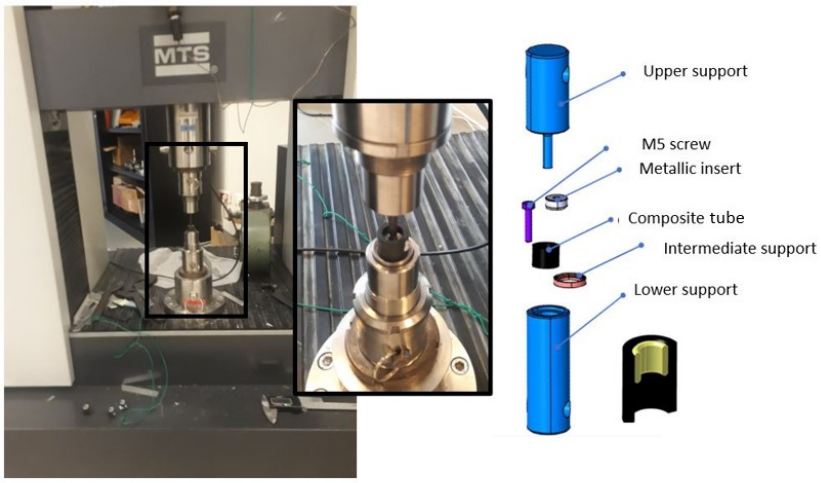

Figure 12. Test setup of the Push through test; the upper support moves downwards to push the intermediate out from the composite tube; the required force to remove it as well as the displacement are registered

8.3. Test results

A typical test result is shown in Figure 13. The typical curve starts with a pre-displacement where the intermediate will theoretically return to its position if the applied force is removed. The curve shows the maximum value of the force that forms a landing, recorded as the PTF.

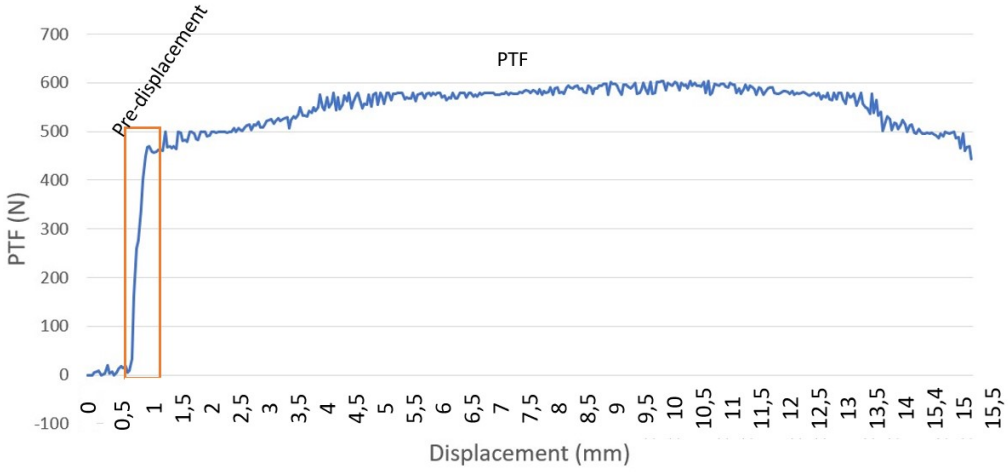

Figure 13. Result curve of the PTF test- $d = 12mm$, $e = 4mm$, $v_f = 10\%$

The experimental PTF was registered and compared to the theoretical value calculated through the equation 28. Two zones were identified in the specimen of Figure 11-b. The specimens that originate from the upper side of the specimen showed a deviation of 20% between experimental and theoretical data; whereas specimens originating from its lower part had a deviation up to 27.2%.

The causes of these deviations are mostly attributed to unaccounted parameters in the equation 28 such as surface rugosity, temperature, porosity, and experimental conditions. This article will further investigate the presence of pores in the molded material.

9. Porosity evaluation and mathematical model enhancement

Porosity is defined as having small voids in the materials. In fact, air bubbles are common in composites and inevitable. Their presence has a negative effect on the mechanical

properties. In fact, 1% of air bubble presence in composite materials reduces the tension strength by 3%, bending strength by 30%, and impact strength by8% [23]. Therefore, each industry defines its own acceptable threshold. In aerospace, for example, the maximum allowable porosity is 2% [24].

A quantitative analysis of the material porosity is then essential. In fact, the density of the composite material is defined as:

$$\rho_{comp} = \frac{\rho_f V_f + \rho_m V_m}{V_f + V_m} \tag{30}$$

where V_f and V_m are the volumes of fiber and matrix, respectively. Due to the presence of porosity, the equation 30 can be re-written as:

$$\rho_{comp} = \frac{\rho_f V_f + \rho_m V_m}{V_f + V_m + V_p} \tag{31}$$

where V_p is the volume of pores in the material.

Porosity can be assessed using non-destructive or destructive methods. Non-destructive Evaluation methods (NDE) include ultrasonic testing, radiography testing, and flash thermography. Ultrasonic testing is commonly used in the industry, it consists of multiple scans of the material in which spherical pores can be evaluated. Pore spheres that have a diameter smaller than the instrument's resolution cannot be detected [25], which determines its precision. The specimen for X-ray tomography is placed between the X-ray source and the detector on a rotary machine. This method detects defects with a diameter up to $1\mu m$ [26]. Flash thermography evaluates porosity through thermal diffusivity. This method is recently being combined with infrared cameras that monitor the temperature variation in the material[25]. Destructive evaluation includes density measurement, matrix digestion, and microscopy testing, [27]. Density evaluation consists of a comparison between Archimedes' theoretical density value and the actual density. This method is complicated as it requires a specific knowledge of the material's matrix and fiber characteristics and volumes. Another method is matrix burn digestion, which uses acid to break down the matrix and reduce the sample to its fiber content. Microscopy is a visual characterization of the sample with a 2-D cross-section analysis. This method is relatively simpler than the above and is widely used.

9.1. Porosity evaluation in composite specimens- Destructive test

In this paper, a destructive method will be deployed. It consists of a photographic/ microscopic analysis of cross-sections of the specimens to determine the porosity percentage.

9.1.1. Specimen preparation and test

The composite tubes used in the PTF evaluation test of the section 8 were fractured. The fractured surfaces were photographed using a Dino lite AM-4013MTL digital microscope. A quantitative analysis was then performed on MATLAB (Figure 14). Each specimen was photographed on its longitudinal section. The variation in light reflection on the broken surface causes light areas at the holes and dark areas at flat surfaces, revealing the pores' presence. Therefore, the photo is first transformed into grayscale. Subsequently, the photo is binarized at the threshold of 0.5, turning bright areas into white and dark areas into black. The fill percentage "k" is then introduced as the percentage of black over the number of pixels of the photo.

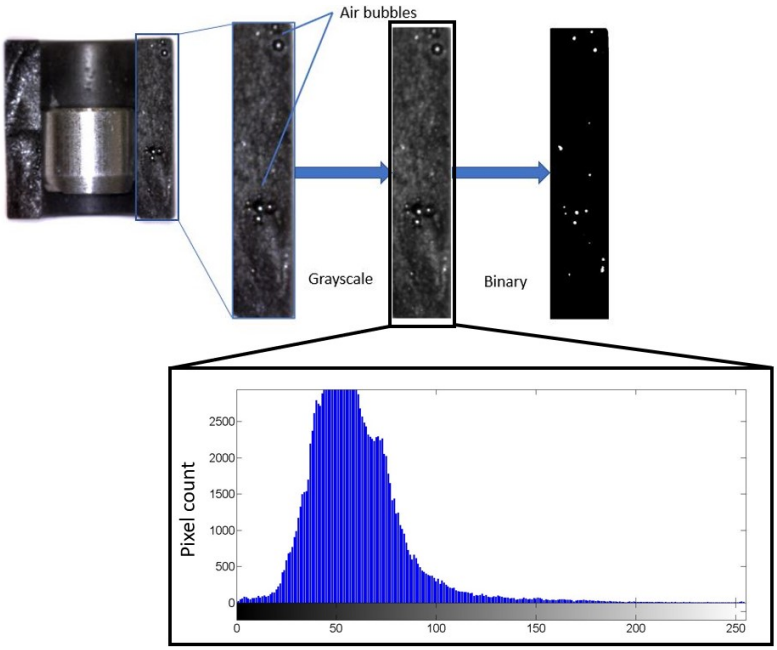

Figure 14. An enlargement of the composite cross-section reveals trapped air in the thickness of the composite material, the photo is grayscaled, and its binarization allows to identify the number of bubbles and their dimensions

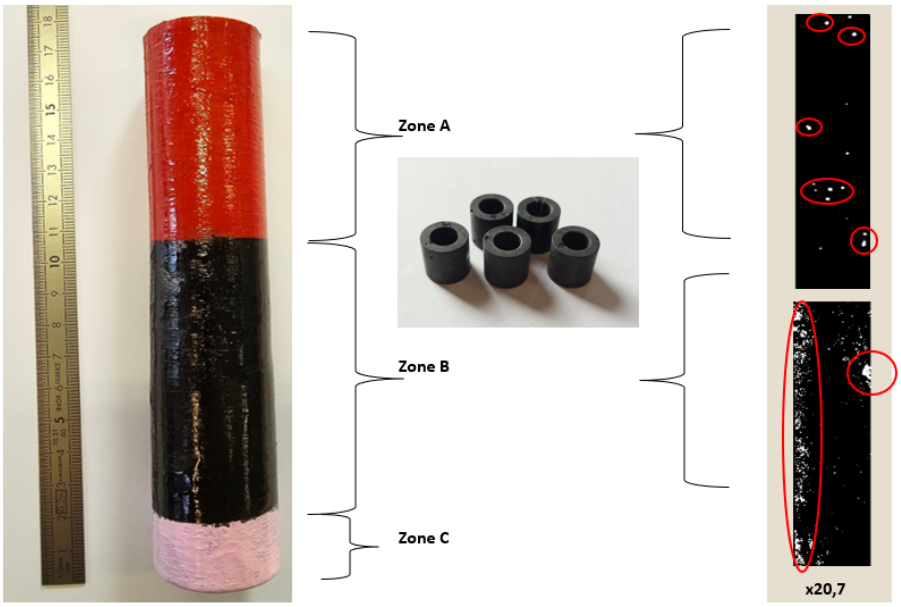

Figure 15. Typical tube specimen; Zone A represents the top zone of the specimen, and zone B is the bottom zone. A cross-section of specimens increased by 20.7 times shows higher porosity in specimens taken from zone B than specimens of zone A.

Referring to Figure 15, zone A represents the top part of the initial molded tube specimen, zone B is the lower part, and zone C is the part fixed to the turning machine when manufacturing the small composite tubes (Figure 11-c). Therefore, no specimens were manufactured from zone C. The cross-section of these tubes, enlarged 20.7 times, reveals the presence of pores highlighted in red. It was noticed that a higher concentration of pores is located in zone B, while zone A specimens exhibited less amount of pores.

Recalling the equation 24, W_{comp}, the denominator of the equation represents the cross-section of the composite material tube. The presence of porosity reduces this section. Therefore, equation 24 can be written as a function of the factor "k."

$$W_{comp} = \frac{\pi(R^2 + R_{o2}^2)}{\pi k(R^2 - R_{o2}^2)} \tag{32}$$

Hence the equation 26 is rectified with the correction factor "k".

$$P = \frac{\delta_r}{\left(R\left[\frac{1}{E_{comp}}\left(-\frac{W_{comp}}{k} + v_{comp}\right) + \frac{1}{E_i}(W_i - v_i)\right]\right)} \tag{33}$$

The equation 33 represents the pressure applied on the intermediate to hold it in position. It is proportional to PTF. The analysis of this equation shows that the factor "K" decreases its theoretical value, which in turn decreases the deviation value between the experimental data and the theoretical results.

9.1.2. Results analysis

#	intermediate material	$2R_{i2}$ (mm)	$2R_{02}$ (mm)	$2R_{01}$ (mm)	l (mm)	$PTF - E$ (N)	$PTF - T$ (N)	$PTF - C$ (N)
$T1$	*Steel*	8.1	14	8.02	5	717	884.8	881.2
$T2$	*Steel*	16.17	24.1	16	5	1475	1482.5	1476.3
$T3$	*Steel*	16.17	24	16	5	1437	1475.2	1469
$T4$	*Steel*	16.18	24	15.99	5	1482	1566.5	1559.9
$T5$	*Steel*	12.07	20	12	5	604	727	723
$T6$	*Steel*	12.06	20	12	5	593	623.1	620
$T7$	*Steel*	12.2	20	12.05	5	1305	1548.4	1542
$T8$	*Brass*	8.1	14.07	8	5	1100	1110.8	1099.2
$T9$	*Brass*	7.99	14.07	8.15	5	1130	1223.7	1211
$T10$	*Aluminum*	8.14	14.08	8.06	5	741	869.1	865.7
$T11$	*Aluminum*	8.1	14.02	8.06	5	1128	1313	1299.5
$T12$	*Steel*	16.15	22.14	16	5	911	1083.7	1060.9
$T13$	*Steel*	16.15	22.12	16.03	5	806	860.6	842.5
$T14$	*Steel*	16.22	24.05	16.1	5	953	1033.6	1012.2
$T15$	*Steel*	12.1	18	12.04	5	416	517.6	507

Table 2. PTF test results

The evaluation of the specimens' porosity percentage revealed that the pores' volume average was 1.2% for specimens originating from part A and 2.3% for specimens originating from part B. This was due to the imprisonment of air bubbles at the cylinder tube specimen's lower part (Part B) during the curing process. It is then worth noting that the porosity evaluation revealed a limitation on the feasible molding thickness; where the process must be revised for parts with high thickness. Table 2 displays the obtained results; where PTF-T represents the theoretical results according to the equation 24 and the column PTF-C represents the results according to the corrected equation resulting from the calculated pressure equation 33. Specimens (T1-T11) were taken from part A, and specimens (T12-T15) from part B. Knowing that the average porosity percentage is 1.2% for specimens T1-T11, the correction factor is $k = 0.988$; for specimens T12-T15, the average porosity percentage is 2.3% therefore the correction factor is $k = 0.977$. The application of the correction factors results in a decrease between the experimental data and theoretical value by almost 0.5% (T1-T11) and 1.8% (T12-T15).

10. Discussions

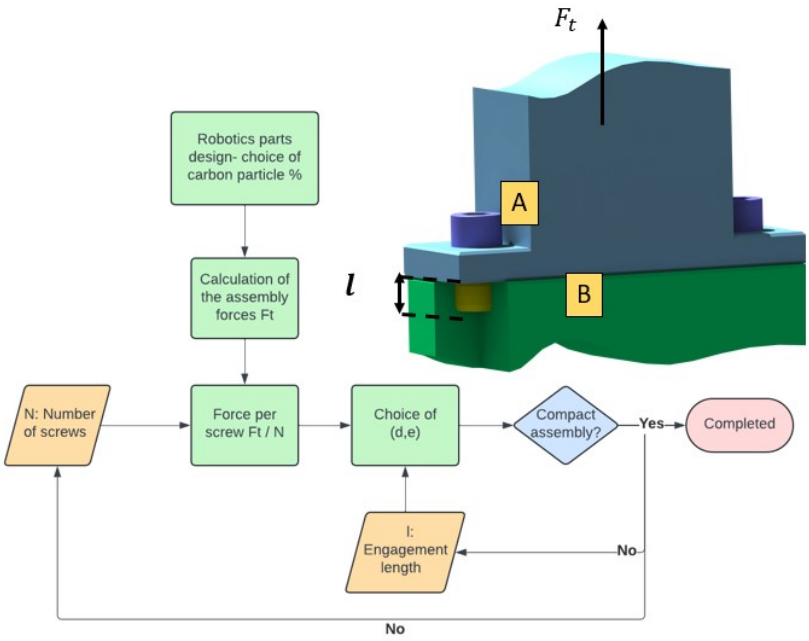

Figure 16. EPATH geometric values choice procedure

The development of the EPATH provides a solution for hydraulically integrated robotic components assembly. Choosing suitable parameters is depicted in the flowchart of Figure 16. It starts with the robotic part's design and determining the required volume of carbon particle percentage. Once the parts are designed, the required assembly forces are calculated (F_t). Then, the force is calculated per screw as: $\frac{F_t}{N}$ with N representing the number of screws in the assembly zone. The charts are then used to determine the values d, e, l. The Figure 17 chart represents the PTF per 1 mm of engagement length. The charts are designed to compensate for the maximum porosity existing in the composite. Depending upon the mechanical design of the robotic part, a length l is first chosen. Consequently, a pair of (d, e) can be selected from the graphs. As an example, suppose that a total force $F_t = 4500N$ is required at the assembly zone and that $N = 6$ screws are used. A choice of engagement length of $5mm$ means that the intermediate's length is $l = 5mm$. Therefore the required

$$PTF = \frac{F_t}{NL} = \frac{4500}{6 * 5} = 150N/mm \tag{34}$$

Returning to Figure 17, a line is drawn at $150N/mm$, it intersects the curves in five points $(d;e) = (16;3,55)$, $(d;e) = (14;3,8)$, $(d;e) = (12;4,15)$, $(d;e) = (10;4,85)$, and $(d;e) = (8;6,7)$. Depending upon the design geometric limitation, one of the combinations can be chosen, or the calculation can be repeated with an engagement length $(l_1 > l = 5mm)$ to further optimize the (d, e) parameters.

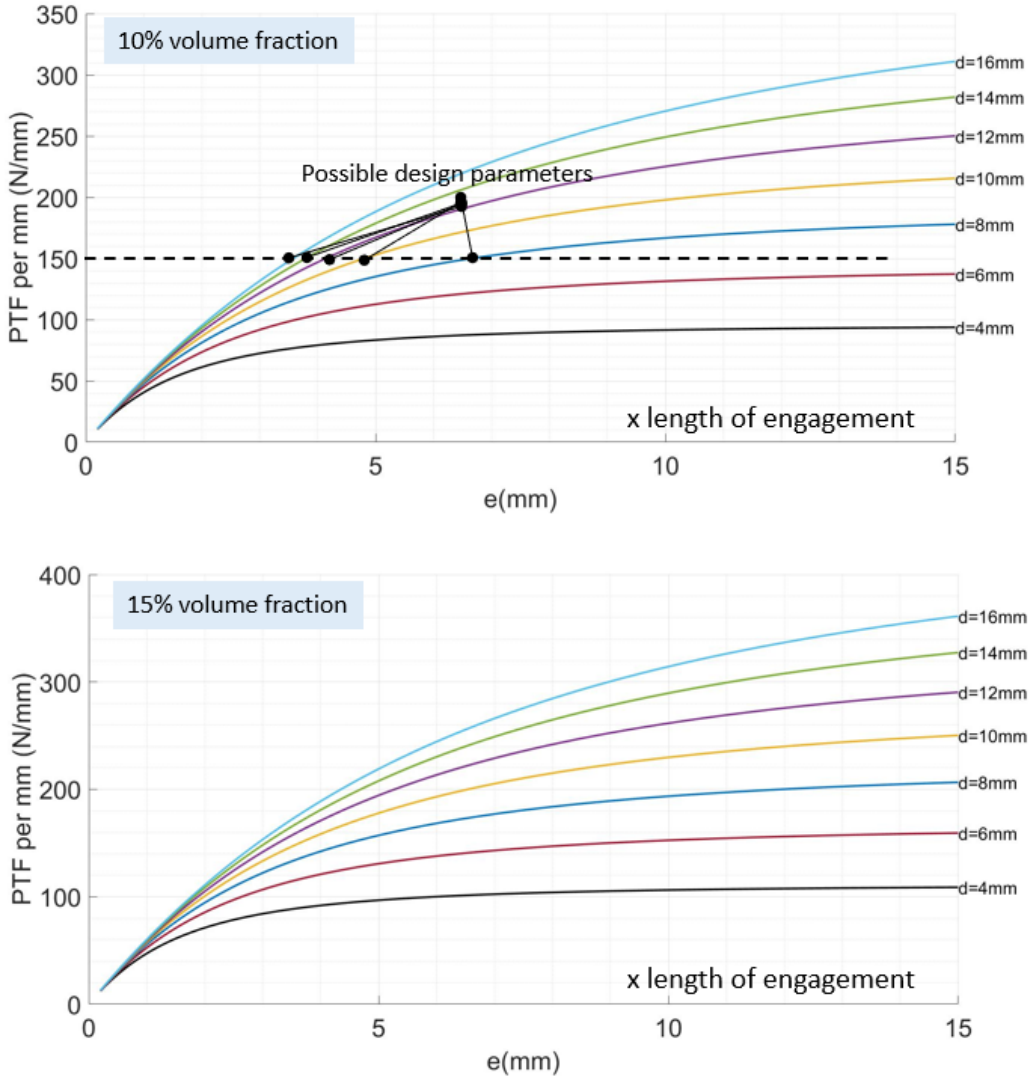

Figure 17. Geometric parameters design choice graphs

11. Conclusions

Using carbon composite materials in developing robotic parts has several advantages, particularly in weight reduction and design flexibility. This technology allows the integration of external hydraulic tubes inside robotic parts to create oil passages for hydraulically actuated robots. However, managing leaks in assembled surfaces presents a significant challenge when implementing this technology in these robots.

This article introduced a novel assembly methodology for hydraulically integrated mechanisms manufactured with carbon composite materials. The developed methodology allowed for a robust, lightweight, and leakproof assembly. The article detailed the mathematical model of 11 parameters for the assembly zone. A numerical simulation on MATLAB permitted to evaluate the effect of these parameters and to set a limitation based on maximum stress supported by the composite material. Experimental validation was carried out to validate the mathematical model; it allowed the detection of pores inside the molded material. The quantification of this porosity was implemented in a correction factor in the mathematical model, and a maximum deviation of 20% was observed. Future research will include optimizing the design parameters to optimize the assembly surface and increase the assembly's strength.

12. List of abbreviations

Symbol	Description	Unit
E_i	Young modulus of intermediate's material	N/m^2
E_f	Young modulus of particles	N/m^2
E_m	Young modulus of the matrix	N/m^2
E_{comp}	Young modulus of the composite material	N/m^2
ϵ_t	Hoop strain	m/m
ϵ_r	Radial strain	m/m
σ_t	Hoop stress	N/m^2
σ_r	Radial stress	N/m^2
P	Exerted pressure at the interference fit area	N/m^2
F	Axial force applied on the intermediate	N
R	Radius at the interference fit	m
d	Interference fit diameter	m
R_{i1}	Intermediate's internal radius	m
R_{o1}	Intermediate's external radius	m
R_{i2}	composite tube internal radius	m
R_{o2}	composite tube external radius	m
l	intermediate's length	m
μ_K	Friction coefficient between assembled materials	
k_f	particle efficiency parameter	
k	Filling percentage of the composite	
v_f	particle volume fraction	
v_i	Poisson ratio of the intermediate's material	
v_{comp}	Poisson ratio of the composite material	

Author Contributions: Conceptualization, M.Sleiman. and S.AlFayad.; methodology, M.Sleiman. and K. Khalil; software, M.Sleiman, and A.Olaru.; validation, M.Sleiman; formal analysis, M.Sleiman; investigation, M.Sleiman; resources, M.Sleiman and S. AlFayad; data curation, M.Sleiman, and A.Olaru.; writing—original draft preparation,M.Sleiman; writing—review and editing, K. Khalil, S. AlFayad; visualization, M.Sleiman, and A.Olaru.; supervision, K. Khalil, S. AlFayad; project administration, S.AlFayad.; funding acquisition, S.AlFayad. All authors have read and agreed to the published version of the manuscript.

Funding: This work was funded by KALYSTA Actuation and the Industrial Excellence Chair between KALYSTA Actuation and the University of Evry.

Conflicts of Interest: The authors declare no conflicts of interest.

References

1. Nelson, G.; Saunders, A.; Playter, R. The PETMAN and Atlas Robots at Boston Dynamics. *Humanoid Robotics: A Reference* **2017**, pp. 1–18. https://doi.org/10.1007/978-94-007-7194-9_15-1.
2. Whitman, E.C. Robust Optimal Walking on the Sarcos Humanoid Robot. Phd thesis, Citeseer, 2012.
3. Abdellatif, A.; Alfayad, S.; Hildebrandt, A.C.; Ouezdou, F.B.; Mechbal, N.; Zweiri, Y. Development of a New Hydraulic Ankle for HYDROïD Humanoid Robot. *Journal of Intelligent and Robotic Systems: Theory and Applications* **2018**, *92*, 293–308. https://doi.org/10.1007/s10846-017-0750-z.
4. Alfayad, S.; Ouezdou, F.B.; Namoun, F. Humanoid robot implementing a spherical hinge with coupled actuators, 2014.
5. Alfayad, S.; KARDOFAKI, M.; SLEIMAN, M.; Arlot, R. Verin a capteur de position integre, 2023.
6. Alfayad, S.; Kardofaki, M.; Sleiman, M. Actionneur hydraulique à compensation de surpression. PCT/EP2020/054895, 2020.
7. Alfayad, S.; Ouezdou, F.B.; Namoun, F.; Bruneau, O.; Henaff, P. Three DOF hybrid mechanism for humanoid robotic application: modeling, design and realization. In Proceedings of the 2009 IEEE/RSJ International Conference on Intelligent Robots and Systems. IEEE, 2009, p. 4955–4961.
8. Alfayad, S.; Tayba, A.M.; Ouezdou, F.B.; Namoun, F. Kinematic synthesis and modeling of a three degrees-of-freedom hybrid mechanism for shoulder and hip modules of humanoid robots. *Journal of Mechanisms and Robotics* **2016**, *8*, 041017.
9. Dynamics, B. Boston Dynamics ' Marc Raibert on Next - Gen ATLAS : " A Huge Amount of Work " The founder of Boston Dynamics describes how his team built one of the **2016**.

10. Barasuol, V.; Villarreal-Magaña, O.A.; Sangiah, D.; Frigerio, M.; Baker, M.; Morgan, R.; Medrano-Cerda, G.A.; Caldwell, D.G.; Semini, C. Highly-integrated hydraulic smart actuators and smart manifolds for high-bandwidth force control. *Frontiers Robotics AI* **2018**, *5*. https://doi.org/10.3389/frobt.2018.00051.
11. El asswad, M. Nouvelles méthodologies pour les robots humanoïdes intégrés hydrauliques légers. These de doctorat, Université Paris-Saclay (ComUE), 2018.
12. de Freitas, S.A.; Vieira, J.T.; Brandão, L.C. Experimental investigation of tapping in CFRP with analysis of torque-tension resistance. *The International Journal of Advanced Manufacturing Technology* **2019**, *104*, 757–766.
13. Tsao, C.C.; Hocheng, H. Effect of tool wear on delamination in drilling composite materials. *International journal of mechanical sciences* **2007**, *49*, 983–988.
14. Lee, J.H.; Ge, J.C.; Song, J.H. Study on burr formation and tool wear in drilling CFRP and its hybrid composites. *Applied Sciences* **2021**, *11*, 384.
15. Yenigun, B.; Kilickap, E. Prediction of the tensile load of drilled CFRP by artificial neural network. *Applied Sciences* **2018**, *8*, 549.
16. Ebnesajjad, S.; Landrock, A.H. *Adhesives technology handbook*; William Andrew, 2014.
17. Sleiman, M. New actuation technologies for humanoid robotics and assistive devices. These de doctorat, université Paris-Saclay, 2022.
18. Vullo, V.; Analysis, S. *Circular Cylinders and Pressure Vessels Stress Analysis and Design*; Springer Series in Solid and Structural Mechanics 3, 2014.
19. Callister, W. *Materials science and engineering : an introduction , Jr.—7th ed. p. cm.,TA403.C23 2007, John Wiley Sons*; John Wiley Sons, Inc., 2007. https://doi.org/10.1016/0025-5416(87)90343-0.
20. Madej, J.; Śliwka, M. Analysis of Interference-Fit Joints. *Applied Sciences* **2021**, *11*, 11428.
21. Standard, I. ISO 527-4:2023.
22. Easycomposite. IN2 Epoxy Infusion Resin - Easy Composites.
23. Aaboud, B.; Bizet, L.; Saouab, A.; Nawab, Y. Effect of the spatial variation of permeability on air bubble creation and compression. *Journal of Reinforced Plastics and Composites* **2020**, *39*, 285–298. https://doi.org/10.1177/0731684419899475.
24. Shoukroun, D.; Massimi, L.; Endrizzi, M.; Nesbitt, A.; Bate, D.; Fromme, P.; Olivo, A. Quantification of porosity in composite plates using planar X-ray phase contrast imaging. *NDT E International* **2023**, *139*, 102935.
25. Meola, C.; Toscano, C. Flash thermography to evaluate porosity in carbon fiber reinforced polymer (CFRPs). *Materials* **2014**, *7*, 1483–1501.
26. Kastner, J.; Plank, B.; Salaberger, D.; Sekelja, J. Defect and porosity determination of fibre reinforced polymers by X-ray computed tomography. In Proceedings of the 2nd International Symposium on NDT in Aerospace. NDT Hamburg, Germany, 2010, p. 1–12.
27. Little, J.E.; Yuan, X.; Jones, M.I. Characterisation of voids in fibre reinforced composite materials. *Ndt E International* **2012**, *46*, 122–127.